Sensors and Materials, Vol. 38, No. 11 (2026) 6371–6400
MYU Tokyo

S & M 4686

Automatic Jumper Length Extraction from Light Detection and Ranging (LiDAR) Point Cloud Data of Transmission Towers and Assessment of Wind Deflection Safety Margin

Xiaofan Liu,[1] Jiao Zhu,[1] Chengfei Zhang,[1] and Xu Wang[2*]

[1]State Grid Jiangsu Electric Power Co., Ltd. Construction Branch, Nanjing 210009, China
[2]Yancheng Institute of Technology, Yancheng 224051, China

(Received July 7, 2026; accepted September 30, 2026)

Keywords: transmission tower jumper, LiDAR point cloud, catenary curve fitting, wind deflection, safety margin

The reliability of transmission lines under wind loads largely depends on adequate electrical clearances around jumpers. Although the automatic extraction of jumper geometry from light detection and ranging (LiDAR) point clouds and the quantitative assessment of clearance risks under wind deflection are important, a complete, reproducible computational workflow is still lacking. In this paper, we present a procedure for estimating jumper conductor length from airborne LiDAR data and evaluating clearance risks under wind deflection. First, multiscale feature descriptors are used to classify the point cloud around each tower and separate jumper points from tower lattice members and ground returns. Then, the 3D trajectory of the jumper conductor is reconstructed using the exact catenary solution, and the conductor length is obtained directly from its closed-form expression, avoiding the inherent inconsistency in the arc length parameterization of the original parabolic approximation under constant tension. Finally, the reconstructed geometry is used as input to a structural mechanics model. Numerical simulation determines the lateral displacement of the jumper assembly under a specified wind pressure distribution and yields a dimensionless safety margin index, defined as the ratio of the remaining clearance to the required clearance. To address incomplete point clouds caused by occlusion and uneven scanning density, we use iteratively reweighted least squares to stabilize the fitting process. The method is validated on three transmission lines covering different tower types, jumper layouts, and terrains. On the independent validation set, the precision, recall, and F1 score are 0.971, 0.946, and 0.958, respectively, and Cohen's kappa is 0.955. The mean absolute error and root mean square error of length extraction are 21.4 and 28.7 mm, respectively, and the median relative error is 0.42%. Propagating the uncertainty in the safety margin yields a clearance violation probability, replacing the original deterministic classification into three levels with a probabilistic classification. For a span with a safety margin point estimate of 1.059, the clearance violation probability still reaches 0.320, demonstrating the risk of judging compliance solely from a point estimate. These results provide a quantitative basis for

*Corresponding author: e-mail: xuwwang@yeah.net
https://doi.org/10.18494/SAM6506

ISSN 0914-4935 © MYU K.K.

maintenance teams to prioritize jumper maintenance and plan targeted measures to mitigate wind deflection.

1. Introduction

Transmission lines are critical infrastructure for economic activity and public safety. At tension and terminal towers, jumper conductors connecting adjacent spans are among the vulnerable components.[1,2] Jumpers are usually made of the same material as the main conductors, with sufficient sag to accommodate temperature changes, structural displacement, and vibration induced by wind. This sag is mechanically necessary but gives the jumper a complex three-dimensional shape that is difficult to assess accurately by conventional visual inspection.[3] Under strong crosswinds, the jumper moves toward the grounded tower structure, reducing the air clearance required for insulation. When the remaining clearance falls below the minimum specified in the operating procedures, the risk of flashover increases significantly, potentially triggering protective devices and unplanned outages.[4,5]

Current jumper clearance checks rely on manual measurements during ground or tower inspections, supplemented by approximate geometric calculations. Operators measure jumper length and lateral clearance using a laser rangefinder or an insulated measuring rod and compare the results with design drawings and clearance standards. This approach has several recognized limitations: jumpers near the top of a tower are difficult to access, measurement accuracy depends on operator experience and observation position, and 2D field measurements cannot fully capture the 3D geometry that determines clearance under different wind loads.[6,7] In addition, manual inspections capture only the state at the time of measurement and cannot evaluate performance under other wind conditions.

Airborne LiDAR scanning has become a routine method for mapping transmission corridors, enabling jumper assessment to move from a manual, qualitative, and fragmented process to an automated, quantitative, and reproducible workflow. LiDAR systems carried by helicopters and unmanned aerial vehicles can acquire point clouds with more than 50 points per square meter across an entire corridor, capturing the three-dimensional geometry of tower members and conductors.[8,9] The technical challenge lies in extracting engineering information from these large point clouds, particularly in identifying sparse jumper points among dense returns from tower members, insulator strings, and vegetation, and in constructing continuous geometric models for length calculation and wind deflection simulation.[10]

Existing point cloud processing methods for transmission facilities mainly address main phase conductors and ground wires. These conductors follow a simple catenary over long spans and are well characterized by dense, regularly distributed LiDAR data. Jumper extraction is much more difficult. Jumper geometry is a composite three-dimensional curve that usually includes a descending section, a lower loop, and an ascending section leading to the terminal connection at the strain clamp. It cannot be described by the single-span catenary model used for main conductors.[11,12] Jumper returns are sparse because the conductor diameter is small relative to the spacing between LiDAR footprints and the conductor surface is often oblique to the scanning plane, reducing the effective backscattering area. In addition, jumpers are close to

dense tower structures, making it difficult to distinguish jumper points from tower points using the spatial position alone.[13]

To clarify the methodological contribution of this study, we review existing work in three research areas. The first is the point cloud segmentation of transmission corridors. Multiscale descriptors and supervised classifiers based on covariance features have been studied extensively. Weinmann et al. presented a general framework for neighborhood scale and feature selection,[14] Demantké et al. addressed scale selection based on dimensionality,[15] and the effectiveness of random forests for these tasks has also been established.[16] These studies typically classify points into four categories: conductors, towers, vegetation, and ground. Jumpers are either included in the conductor class or discarded as noise, without a dedicated class definition or corresponding feature design. The second area is conductor geometry reconstruction. Catenaries and their parabolic approximations are widely used to reconstruct conductors in main spans. Jwa and Sohn proposed automatic power line reconstruction based on a catenary model,[17] and Girard et al. presented real-time sag estimation for UAV inspection.[18] These studies address conductors over long spans with known endpoints and small sag. The error of the parabolic approximation is negligible when the ratio of sag to span is below 0.05. For jumpers, however, this ratio is typically between 0.15 and 0.30, making the approximation unsuitable. The third area is clearance assessment under wind deflection. Swing angle formulas and load combination methods in design codes are well established, and wind deflection warning methods based on digital twins and weather data have also been reported. These methods use design parameters or online meteorological data as input, but take the geometry from design drawings without coupling it to the measured as-built geometry. Consequently, they cannot capture differences in actual geometry caused by construction deviations, conductor creep, and adjustments during commissioning.

Two points follow from this review. First, the multiscale covariance features, random forest classification, the density-based spatial clustering of applications with noise (DBSCAN), and the iteratively reweighted least squares used in this study are established techniques and are not claimed as novel. Second, the methodological contribution comprises three aspects. A dedicated jumper class and a criterion based on the persistence of linearity across scales allow jumper points to be separated from tower points. The arc length parameterization of the exact catenary replaces the parabolic solution under constant tension, making length calculation consistent with the mechanical model and eliminating approximation error over the range of sag to span ratios typical of jumpers. The measured geometry, a structural model of wind deflection, and uncertainty propagation are integrated into a reproducible computational workflow that yields a safety margin and a clearance violation probability. Table 1 shows a comparison of this approach with representative existing methods, and Sect. 4.2 presents quantitative comparisons.

The remainder of this article is organized as follows. Section 2 introduces LiDAR data preprocessing and jumper extraction, including multiscale feature descriptors, classifier configuration, and reproducible parameter settings. Section 3 presents the jumper geometry reconstruction model, the arc length parameterization of the exact catenary, and its closed-form length expression. Section 3.4 presents a complete uncertainty propagation analysis. Section 4 reports validation and baseline comparisons on three operational transmission lines. Section 5 shows a summary of contributions and limitations and future work.

Table 1
Comparison of present work with representative prior studies.

Research line	Representative method	Clearance assessment	Reported capability for jumpers
Corridor point cloud segmentation	Multiscale covariance features with supervised classifier[14,15,16]	None	Jumper merged into conductor class or discarded
Deep segmentation networks[11,13]	Point-based network	None	No jumper class defined
Conductor geometric reconstruction	Catenary-based power line reconstruction	None	Not addressed
Real-time sag estimation for inspection[17,18]	Main span conductor	Not addressed	
Wind deflection assessment	Code-based swing angle and load combination[19]	Deterministic ratio	Design geometry only
Digital-twin-driven wind deflection warning	Line section	Design geometry only	
Present work	Multiscale features with random forest, exact catenary reconstruction, propagated uncertainty	Probabilistic margin with clearance violation probability	As-built geometry from LiDAR

2. LiDAR Point Cloud Preprocessing and Jumper Point Extraction

Extracting jumper points from raw LiDAR point clouds provides the basis for subsequent geometric reconstruction and wind deflection analysis. The raw airborne LiDAR data collected over a transmission corridor include returns from terrain, vegetation, buildings, towers, insulator assemblies, ground wires, phase conductors, and jumpers. Preprocessing reduces the data to point sets relevant to jumper geometry, after which classification separates jumper returns from other points near the tower structure.

Preprocessing begins with progressive morphological filtering to distinguish ground returns from nonground returns. Ground points are needed to construct a digital terrain model but do not provide information about jumper geometry, so they are excluded from subsequent processing. The remaining nonground points are partitioned by individual tower using the tower coordinates in the asset database. To ensure reproducibility, Table 2 shows all preprocessing parameters and the basis for selecting them. The horizontal half-width of the bounding volume is determined by the maximum jumper displacement under design wind conditions plus a 1.0 m allowance based on the measured variability in jumper swing.

2.1 Multiscale feature descriptor for jumper discrimination

Jumper conductor points are distinguished from other points within the tower bounding volume using geometric features that capture differences between slender, curved jumpers and the lattice structure of tower steelwork.[18] For each point, a feature vector describes the geometry at several spatial scales, allowing the classifier to consider both local surface properties and the surrounding structure.

Table 2
Preprocessing parameters and their determination.

Parameter	Symbol	Value	Determination
Morphological filter maximum window size	W	20 m	Largest nonterrain object in corridor
Morphological filter slope threshold	S	0.30	Steepest terrain in Corridor C
Elevation difference threshold	DH	30 m	Twice the vertical point accuracy
Bounding volume horizontal half-width	B	4.5 m	Maximum design swing plus 1.0 m allowance
Bounding volume lower bound	Z	Lowest jumper clamp minus 2.0 m	Asset database attachment height
Bounding volume upper bound	Z	Tower top	Asset database tower height
Duplicate point tolerance	D	0.01 m	Sensor range resolution
Number of points retained per tower (mean)	N	24 316	Result for three corridors

For a point p_i with coordinates (x_i, y_i, z_i) inside the tower bounding volume, a spherical neighborhood $\mathcal{N}(p_i, r_k)$ of radius r_k is defined. The point distribution in this neighborhood is described by the eigenvalues $\lambda_1 \le \lambda_2 \le \lambda_3$ of the covariance matrix:

$$\Sigma(p_i, r_k) = \frac{1}{\left|\mathcal{N}(p_i, r_k)\right|} \sum_{p_j \in \mathcal{N}(p_i, r_k)} \left(p_j - \overline{p}\right)(p_j - \overline{p})^T , \tag{1}$$

where $\left|\mathcal{N}(p_i, r_k)\right|$ represents the number of points in the neighborhood, p is the centroid of the points in the neighborhood, and the superscript T denotes the transpose of a vector. The eigenvalues of the covariance matrix indicate the scatter of the points in three mutually perpendicular principal directions, with λ_1 indicating the variance in the direction of least scatter and λ_3 indicating the variance in the direction of greatest scatter.

From the eigenvalues, local shape descriptors are derived to quantify the geometric characteristics of the point distribution. The linearity measure L_λ indicates the degree to which the points are arranged along a one-dimensional structure, the planarity measure P_λ indicates the degree to which the points lie on a two-dimensional surface, and the scattering measure S_λ indicates the degree to which the points are distributed volumetrically.

$$L_\lambda = \frac{\lambda_3 - \lambda_2}{\lambda_3},\ P_\lambda = \frac{\lambda_2 - \lambda_1}{\lambda_3},\ S_\lambda = \frac{\lambda_1}{\lambda_3} \tag{2}$$

These three measures are nonnegative and sum to unity by construction, providing a normalized representation of local shape that is invariant to the absolute scale of the point distribution. Jumper conductors, being slender cylindrical objects, produce point distributions with high linearity and low planarity and scattering. Tower lattice members also produce linear point distributions when considered at small neighborhood radii, but the intersection of multiple lattice members at connection nodes produces planar or volumetric distributions that differ from the consistently linear character of jumper points.[19,20]

The distinction between jumper and tower points becomes more pronounced when the shape descriptors are computed at multiple neighborhood radii $r_k \in \{r_1, r_2, r_3\}$ with $r_1 < r_2 < r_3$. At the smallest radius, the individual tower lattice members and the jumper conductor segments exhibit similar linearity. At medium and large radii, the tower neighborhoods include several intersecting lattice members and connection plates, resulting in increased planarity and scattering measures. In contrast, jumper neighborhoods remain predominantly linear at large radii since the jumper follows a continuous curve without the intersecting structural elements found in the tower. This multiscale behavior provides information for accurately distinguishing jumper points from tower points.

Figure 1 illustrates differences in multiscale geometric properties between tower lattice structures and jumper trajectories. As the neighborhood radius around a tower lattice point increases, more intersecting members are included, shifting the eigenvalue distribution from predominantly linear at small scales to planar or volumetric at larger scales. In contrast, the points in jumper neighborhoods remain predominantly aligned with the conductor trajectory because no additional structural elements intersect it. This distinction is reflected in the variation in linearity across scales: the index approaches unity at all scales for jumper points but decreases monotonically with increasing radius for tower points.

The full feature vector for point p_i concatenates the shape descriptors and additional geometric attributes across the multiscale neighborhood set:

$$f(p_i) = \left[L_\lambda(r_1), P_\lambda(r_1), S_\lambda(r_1), L_\lambda(r_2), P_\lambda(r_2), S_\lambda(r_2), L_\lambda(r_3), P_\lambda(r_3), S_\lambda(r_3), \eta_i, \zeta_i \right]^T, \quad (3)$$

where η_i is the verticality measure computed as the absolute z component of the eigenvector corresponding to the smallest eigenvalue and ζ_i is the local point density defined as the number of points per unit volume within the smallest neighborhood radius. The verticality measure assists in discriminating nearly vertical tower legs from predominantly diagonal jumper segments, while the local point density captures the difference in point sampling density

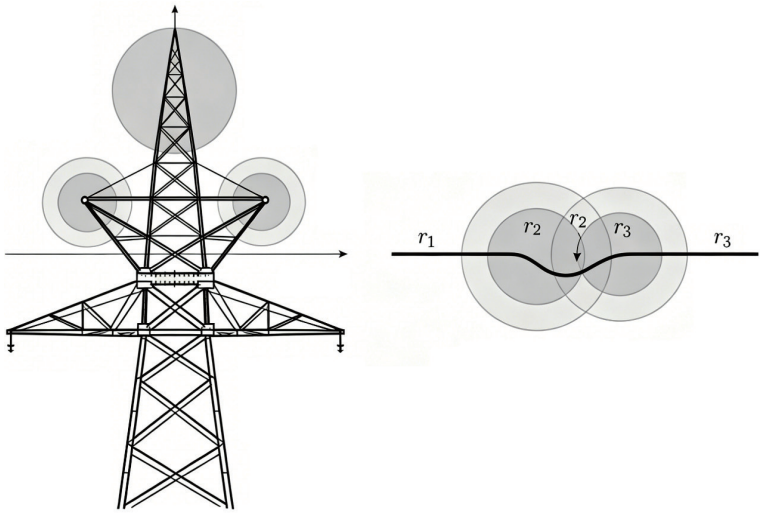


Fig. 1. Multiscale neighborhood analysis of tower lattice structure and jumper conductor geometry.

between the relatively sparse jumper returns and the denser tower structure returns that arise from the larger reflective surface area of the tower steelwork.

2.2 Jumper point classification using ensemble learning

A random forest classifier trained on the multiscale feature vectors classifies points within the tower bounding volume as jumper or nonjumper points. Random forest was chosen because of its ability to handle high-dimensional feature spaces, robustness to irrelevant and redundant features, and ability to provide feature importance measures for interpreting classification decisions.

The training and validation data were obtained from 18 towers on two corridors entirely separate from the case study corridors in Sect. 4. Analysts experienced in transmission line mapping visually labeled each point as a jumper or nonjumper point. During labeling, jumper attachment positions recorded in the asset database constrained the possible locations of jumper points to the region between the strain clamp and the jumper support. To prevent data leakage between the training and validation sets, the data were split by tower rather than by point: 12 towers were used for training and 6 for validation, with both tower types represented in the validation set. Table 3 shows the dataset composition.

Random forest hyperparameters were selected using fivefold cross-validation with grouping by tower within the training subset. Table 4 presents the search grid and selected values.

Table 3
Composition of labeled dataset used for classifier training and validation.

Item	Training subset	Validation subset	Total
Corridors	D and E	D and E	2
Number of towers	12	6	18
Number of lattice dead-end towers	8	4	12
Number of tubular angle towers	4	2	6
Number of points inside bounding volumes	856 314	427 158	1 283 472
Number of labeled jumper points	69 842	35 076	104 918
Number of labeled nonjumper points	786 472	392 082	1 178 554
Jumper class proportion (%)	8.16	8.21	8.17
Number of points used after balanced downsampling	139 684	Not resampled	Not applicable
Manual labeling effort (person hours)	46	23	69

Table 4
Random forest hyperparameters and selected values.

Hyperparameter	Search grid	Selected value	Cross-validation F1 score at selected value
Number of trees T	100, 200, 300, 500, 800	300	0.9569
Maximum depth	10, 15, 20, 25, unlimited	20	0.9569
Number of features per split	2, 3, 4, 6, 11	3	0.9569
Minimum number of samples per leaf	1, 2, 5, 10	2	0.9569
Split criterion	Gini, entropy	Gini	0.9569
Class weight	None, balanced	Balanced	0.9569
Bootstrap sample fraction	0.6, 0.8, 1.0	0.8	0.9569
Number of grid points evaluated	1200	Not applicable	Not applicable
Mean training time per fold (s)	Not applicable	187	Not applicable
Mean inference time per tower (s)	Not applicable	2.4	Not applicable

Selection was based on the mean cross-validation F1 score. When F1 scores were equal, configurations with fewer and shallower trees were preferred to limit inference time.

Algorithm 1 presents the complete point classification and postprocessing procedure, with explicit thresholds to ensure reproducibility.

The random forest classifier with T decision trees produces for each point p_i a class probability estimate $P_{jumper}(p_i)$ that represents the fraction of trees voting for the jumper class. A point is classified as a jumper point if this probability is at least a threshold τ:

$$Class(p_i) = \begin{cases} \text{jumper} & \text{if } P_{jumper}(p_i) \geq \tau \\ \text{nonjumper} & \text{otherwise} \end{cases}, \tag{4}$$

where the threshold τ is selected to balance precision and recall on the validation subset. The classification output for a given tower is a binary labeling of the points within the tower bounding volume, partitioning the point set into jumper candidate points and excluded points. The effects of the threshold on the classification metrics and downstream length extraction are shown in Table 5, from which the value 0.70 is selected as the best compromise between precision and length accuracy. The confusion matrix obtained at this threshold is given in Table 6, and the corresponding metrics broken down by tower type are given in Table 7.

Algorithm 1
Jumper point classification and postprocessing.

Line	Operation
1	Input: point set Q inside the tower bounding volume; radii R, R, R M; trained forest f; threshold tau = 0.70; minimum component size n; maximum clamp distance D M
2	Build a KD tree on Q
3	For each p in Q and each radius r: compute covariance eigenvalues using Eq. (1) and shape descriptors using Eq. (2)
4	Assemble the feature vector using Eq. (3); replace features for neighborhoods with fewer than 5 points by the median conditional on class
5	Evaluate the class probability as the fraction of trees in f voting for the jumper class
6	Assign the jumper label where the class probability is at least tau, using Eq. (4)
7	Extract connected components of points labeled as jumpers using a Euclidean radius of 0.35 m
8	Discard components with fewer than n points
9	Discard components whose centroid lies farther than D from the nearest strain clamp recorded in the asset database
10	Output: candidate jumper point set and the set of rejected points retained for inspection

Table 5
Threshold sweep on validation subset and its effect on downstream length extraction.

Threshold tau	True positives	False positives	False negatives	Precision	Recall	F1 score	Length *RMSE* (mm)
0.50	34 412	2 914	664	0.9219	0.9811	0.9506	41.6
0.60	33 925	1 802	1 151	0.9496	0.9672	0.9583	32.9
0.70	33 168	986	1 908	0.9711	0.9456	0.9582	28.7
0.80	31 904	562	3 172	0.9827	0.9096	0.9447	33.5
0.90	29 655	281	5 421	0.9906	0.8454	0.9123	47.2

Table 6
Confusion matrix on validation subset at selected classification threshold of 0.70.

Predicted class versus reference	Jumper	Nonjumper	Row total
Jumper	33 168	986	34 154
Nonjumper	1 908	391 096	393 004
Column total	35 076	392 082	427 158
Overall accuracy	0.9932	Cohen's kappa	0.9545

Table 7
Classification metrics by tower type on validation subset at selected classification threshold of 0.70.

Tower type	Number of towers	Number of reference jumper points	Precision	Recall	F1 score	Dominant error source
Lattice dead-end	4	22 288	0.9657	0.9375	0.9514	Lattice members in crossarm area parallel to jumper
Tubular angle	2	12 788	0.9805	0.9598	0.9700	Sparse returns on lower loop
All towers	6	35 076	0.9711	0.9456	0.9582	Not applicable

Classification performance depends on the informativeness of the feature set and the representativeness of the training data. Permutation importance was evaluated for the trained random forest, and the results are shown in Table 8. Linearity at the largest neighborhood radius and local point density contribute the most, together accounting for 49.7% of total importance. This supports the interpretation that the persistence of linearity across scales and differences in sampling density are the main geometric features distinguishing jumpers from towers. This finding is consistent across both tower types. However, in the tower crossarm area, discrimination becomes more difficult when tower members are parallel to the jumper trajectory, and verticality becomes the main distinguishing feature. This also explains the slightly lower recall for lattice towers.

Postprocessing addresses two common failure modes of pointwise classification. First, local geometric ambiguity can cause jumper points to be misclassified as nonjumper points, fragmenting an otherwise continuous point set. A spatial connectivity filter extracts connected components of the jumper class and removes those containing fewer than 15 points, on the assumption that a valid jumper assembly forms a continuous cluster exceeding this minimum size. Second, slender objects mounted on towers, such as bird deterrents and aviation warning markers, can produce elongated point clusters that are mistaken for jumpers. A proximity filter removes candidate components whose centroids are more than 6.0 m from the nearest strain clamp. This threshold is based on the maximum possible jumper length recorded in the asset database. Table 9 presents ablation results for both postprocessing steps. Rejected points are retained separately for manual spot checks, and their spatial distribution is shown in Sect. 4.

The complete process is shown in Fig. 2. First, the pointwise multiscale feature vectors are calculated according to the neighborhood analysis of Eqs. (1) to (3) on the raw point cloud subset in the tower bounding volume.[21–24]

Table 8
Permutation importance of feature set, measured as mean decrease in F1 score over 30 permutations.

Rank	Feature	Mean decrease in F1 score	Standard deviation	Share of total (%)
1	L (R)	0.2841	0.0106	28.4
2	Zeta	0.2131	0.0094	21.3
3	L (R)	0.1524	0.0081	15.2
4	Eta	0.0982	0.0063	9.8
5	P (R)	0.0871	0.0058	8.7
6	S (R)	0.0613	0.0047	6.1
7	L (R)	0.0432	0.0039	4.3
8	P (R)	0.0308	0.0031	3.1
9	Remaining three features	0.0298	0.0029	3.0

Table 9
Ablation of postprocessing steps on validation subset at selected classification threshold of 0.70.

Configuration	Precision	Recall	F1 score	Number of spurious clusters per tower	Length *RMSE* (mm)
Pointwise classification only	0.9207	0.9503	0.9353	4.7	46.3
Plus connectivity filter	0.9528	0.9471	0.9499	2.1	35.8
Plus proximity filter	0.9711	0.9456	0.9582	0.3	28.7
Plus both filters without asset database	0.9602	0.9459	0.9530	1.2	31.4

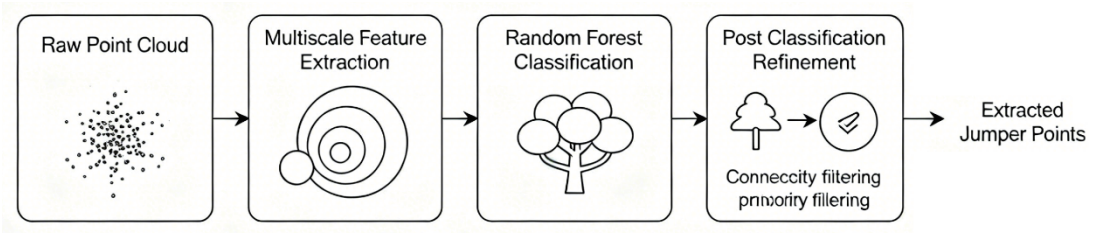


Fig. 2. Processing pipeline for jumper point extraction from LiDAR point clouds near towers.

2.3 Jumper point clustering and span identification

The jumper points extracted by the classification pipeline in Sect. 2.2 form the complete set of jumper returns for a given tower, but these points need to be organized into individual jumper spans prior to the fitting of geometric models. A terminal or angle tower usually supports several jumper assemblies, each connecting a particular phase conductor from the incoming span to the corresponding phase conductor of the outgoing span. The points of different phases are spatially separated, but within the same phase, the jumper may include bundled subconductors resulting in multiple closely spaced point trajectories. The clustering method should classify the points into phase-specific jumper sets and distinguish the subconductor trajectories in each phase bundle.[25,26]

The clustering method uses both spatial proximity and geometric continuity. Table 10 shows the clustering parameters and the basis for selecting them. The parameters are set according to

Table 10
Clustering parameters and their determination.

Stage	Parameter	Corridor A	Corridor B	Corridor C	Determination
Phase separation	DBSCAN radius (m)	0.60	0.60	0.55	One-third of minimum phase spacing
Phase separation	Minimum number of points	12	12	10	Lowest observed return count on one loop
Phase separation	Minimum phase spacing (m)	3.6	4.2	5.0	Design drawing
Subconductor separation	DBSCAN radius (m)	Not applicable	Not applicable	0.18	Two-fifths of bundle spacing
Subconductor separation	Bundle spacing (m)	Not applicable	Not applicable	0.45	Design drawing
Ordering	Graph edge length limit (m)	0.50	0.50	0.45	Three times the median point spacing
Result	Number of clusters per tower (mean)	6.0	6.0	17.8	Observed

the phase spacing and subconductor spacing of each line, without requiring adjustment for individual towers.

Each identified subconductor cluster is ordered along the conductor path to establish a sequential point ordering that respects the physical continuity of the jumper. The ordering procedure constructs a minimum spanning tree on the cluster points using Euclidean distance as the edge weight, then identifies the two endpoints as the points closest to the strain clamp attachment locations. The ordered sequence of points from one endpoint to the other along the minimum spanning tree path provides a one-dimensional parameterization of the jumper trajectory that serves as the basis for curve fitting.

Figure 3 provides an overview of the jumper configuration on a typical transmission tower, illustrating the spatial arrangement that the clustering and span identification procedures must resolve. The three phase jumper assemblies are located vertically on the tower crossarm structure and each phase jumper has a compound three-dimensional trajectory that starts from the strain clamp, descends below the crossarm, forms a loop, and then ascends to the terminating connection. The enlarged inset shows the geometric characteristics of an individual jumper span, such as the asymmetrical loop caused by the different attachment heights and the lateral displacement due to the phase spacing.[27]

3. Jumper Geometry Reconstruction and Wind Deflection Analysis

3.1 3D compound catenary jumper model

The geometry of a jumper conductor under its self-weight is governed by the catenary equation, which describes the equilibrium shape of a perfectly flexible cable with uniform mass per unit length suspended between two support points and subjected to gravitational loading. Unlike main transmission line spans, which traverse distances of typically 200 to 500 m and are well described by a single two-dimensional catenary in a vertical plane, jumper spans traverse much shorter distances with significant three-dimensional curvature introduced by the relative

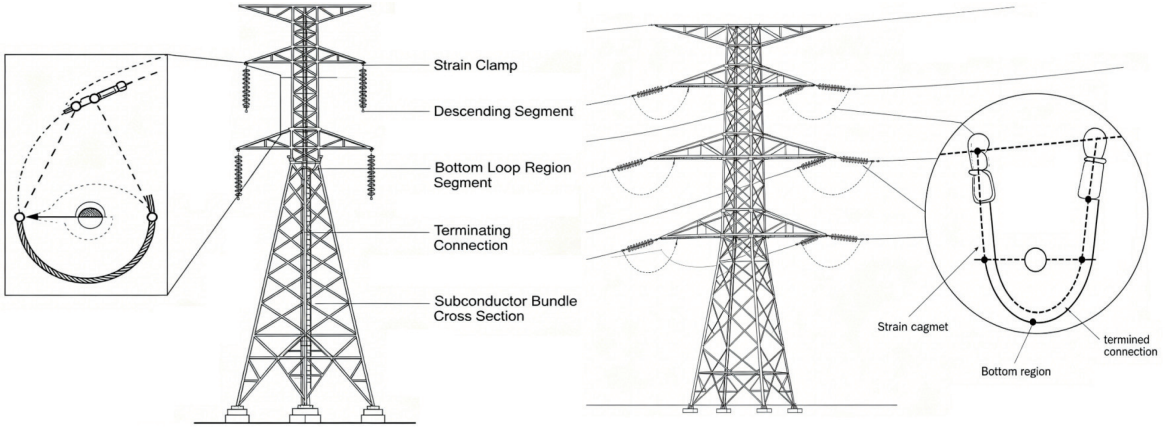


Fig. 3. Transmission tower jumper assembly geometry with phase configuration and subconductor detail.

positions of the attachment points and the requirement to maintain electrical clearance from the tower structure.

The jumper trajectory is modeled as a parametric space curve $\boldsymbol{r}(s) = [x(s), y(s), z(s)]^T$ parameterized by the arc length $s \in [0, L]$, where L is the total conductor length of the jumper. The curve satisfies the vector equilibrium equation for an inextensible cable with uniform weight per unit length:

$$\frac{d}{ds}\left(T(s)\frac{d\boldsymbol{r}}{ds} \right) + w\boldsymbol{k} = 0, \tag{5}$$

where $T(s)$ is the tension magnitude at arc length position s, $d\boldsymbol{r}/ds$ is the unit tangent vector, and $\boldsymbol{k} = [0,0,-1]^T$ is the unit vector in the downward vertical direction. The tension varies along the conductor according to the inclination of the tangent vector, with the highest tension occurring at the upper attachment point where the conductor weight is fully supported.

Let the horizontal unit vector and the vertical unit vector in the load plane be denoted by e_h and e_v, respectively. Since the self-weight acts vertically, the horizontal tension component along the conductor is constant. Taking the lowest point of the curve as the arc length origin, the governing equation is written as

$$T_0 \frac{d^2\boldsymbol{r}}{ds^2} + w\boldsymbol{k} = 0. \tag{6}$$

Integrating Eq. (6) twice with respect to the arc length results in the parametric solution in three dimensions:

$$\boldsymbol{r}(s) = \boldsymbol{r}_0 + \boldsymbol{t}_0 s - \frac{w}{2T_0} s^2 \boldsymbol{k}, \tag{7}$$

where $\boldsymbol{r}_0 = \boldsymbol{r}(0)$ indicates the position vector of the starting attachment point and $\boldsymbol{t}_0 = d\boldsymbol{r}/ds(0)$

denotes the unit tangent vector at this point. The solution gives a parabolic path in the vertical plane determined by the initial tangent vector and the vertical direction, which agrees with the assumption of constant tension. For short jumper spans, the parabolic approximation leads to a small error when compared with the exact catenary and therefore simplifies the parameter estimation.

The jumper model is specified by defining the boundary conditions at the two attachment points. Let $\boldsymbol{r}_A$ and $\boldsymbol{r}_B$ represent the known positions of the strain clamp attachments at the beginning and end of the conductor, respectively. The trajectory of the jumper should satisfy $\boldsymbol{r}(0) = \boldsymbol{r}_A$ and $\boldsymbol{r}(L) = \boldsymbol{r}_B$. Applying these boundary conditions to the parametric solution in Eq. (7), we obtain the constraint

$$\boldsymbol{r}_B = \boldsymbol{r}_A + \boldsymbol{t}_0 L - \frac{w}{2T_0} L^2 \boldsymbol{k} \,. \tag{8}$$

This equation expresses three scalar constraints among the unknown parameters L, T_0, and the two independent components of the unit vector $\boldsymbol{t}_0$, resulting in four unknowns. The system is underdetermined by one degree of freedom, which indicates the physical situation that various combinations of length and tension can give rise to a trajectory connecting the same two endpoints, where smaller lengths require higher tensions and produce less pronounced sag profiles.

The additional condition for determining the specific jumper shape is obtained from the jumper design, which determines the target d_{sag} at the bottom of the jumper loop. The sag is defined as the vertical distance between the horizontal plane of the lower attachment point and the lowest point of the jumper. For the parabolic curve expressed by Eq. (7), the arc length position s_{min} corresponding to the minimum height is determined by

$$\frac{dz}{ds}|_{s=s_{min}} = t_{0z} - \frac{w}{T_0} s_{min} = 0 \,, \tag{9}$$

yielding $s_{min} = T_0 t_{0z}/w$, where t_{0z} is the vertical component of $\boldsymbol{t}_0$. The minimum height is then

$$z_{min} = z_A + t_{0z} s_{min} - \frac{w}{2T_0} s_{min}^2 = z_A + \frac{T_0 t_{0z}^2}{2w} \,. \tag{10}$$

Given the attachment geometry and the given sag, Eqs. (8) to (10) determine the jumper parameters L, T_0, and $\boldsymbol{t}_0$, which describe the continuous path for length calculation and wind deflection analysis.

Table 11 shows that, over the range of sag to span ratios typical of jumpers, the parabolic approximation overestimates length by 0.22 to 2.53%, corresponding to 18.6 to 244.7 mm for an 8.0 m horizontal span. These approximation errors are comparable to or greater than the length extraction root mean square error of 28.7 mm reported in this study. The parabolic approximation is therefore unsuitable for the accuracy target of this study.

Table 11
Deviation of parabolic approximation from exact catenary for horizontal span of 8.0 m.

Ratio of sag to span F/A	Sag F (m)	H/w (m)	Exact catenary length (m)	Parabolic length (m)	Length overestimate (mm)	Relative overestimate (%)	T/h	Tension variation along cable (%)
0.15	1.20	6.858	8.4614	8.4800	18.6	0.220	1.175	17.5
0.20	1.60	5.247	8.7977	8.8533	55.6	0.632	1.305	30.5
0.25	2.00	4.297	9.2063	9.3333	127.0	1.380	1.465	46.5
0.30	2.40	3.676	9.6753	9.9200	244.7	2.529	1.653	65.3

3.2 Robust curve fitting from noisy point data

The jumper parameters are estimated from the extracted point cloud data through a curve fitting procedure that minimizes the geometric deviation between the parametric model and the observed points. The fitting problem is formulated as a nonlinear least squares optimization that adjusts the model parameters to minimize the sum of squared orthogonal distances from the observed points to the model trajectory.

For a cluster of ordered jumper points, the fitting objective function is defined as

$$\varepsilon\left(L,T_0,\boldsymbol{t}_0\right)=\sum_{i=1}^{M}d_i^2\left(L,T_0,\boldsymbol{t}_0\right). \tag{11}$$

Here, d_i is the minimum Euclidean distance from point $\boldsymbol{p}_i$ to the parametric trajectory defined by Eq. (7). The computation of d_i requires solving a one-dimensional minimization problem along the trajectory to find the arc length parameter s_i that produces the closest point on the model to the observed point:

$$s_i=arg\min_{s\in[0,L]}\|\boldsymbol{p}_i-r\left(s;L,T_0,\boldsymbol{t}_0\right)\|^2. \tag{12}$$

This inner minimization is solved by Newton iteration initialized with the arc length estimate obtained from the ordered sequence of points along the minimum spanning tree path. The presence of residual nonjumper points that survive the classification and refinement procedures, as well as the inherent measurement noise in the LiDAR point positions, motivates the use of robust estimation techniques that reduce the effect of outlier observations on the fitted model. An iteratively reweighted least squares scheme is adopted, in which the objective function is modified to include observation weights w_i that are updated at each iteration based on the current residual magnitudes:

$$\mathcal{E}_{robust}\left(L,T_0,\boldsymbol{t}_0;\boldsymbol{w}\right)=\sum_{i=1}^{M}\omega_i d_i^2\left(L,T_0,\boldsymbol{t}_0\right). \tag{13}$$

The weights are computed using the Huber loss function, which assigns unit weight to observations with residuals below a threshold and weights inversely proportional to the residual magnitude for observations exceeding the threshold:

$$\omega_i = \begin{cases} 1 & \text{if } |d_i| \le \delta \\ \delta / |d_i| & \text{if } |d_i| > \delta \end{cases}, \tag{14}$$

where the threshold δ is set as a multiple of the estimated standard deviation of the inlier residuals. The iterative procedure alternates between solving the weighted least squares problem to update the model parameters and recomputing the weights on the basis of the new residuals until convergence.

The robust standard deviation of the inlier residuals is estimated using the median absolute deviation. Algorithm 2 gives the complete iterative procedure, and Tables 12 and 13 report the convergence criterion and observed convergence behavior, respectively.

Figure 4 illustrates the relationship between the extracted jumper point cloud and the fitted parametric trajectory, together with the wind deflection concept that motivates the safety margin analysis. The point cluster shows a jumper loop shape with a higher point density around the attachment areas, where the LiDAR scan geometry is more favorable, and a lower point density in the bottom loop area, where the conductor surface is nearly tangential to the scan direction. The fitted catenary model can describe the whole trajectory of the jumper despite the uneven distribution of points. The right panel illustrates the effect of wind deflection, in which the lateral wind force moves the jumper from its equilibrium position, thereby decreasing the clearance between the conductor and the tower structure.

3.3 Jumper length computation and wind deflection safety margin

Jumper length is calculated by integrating the magnitude of the trajectory derivative between the two endpoint parameter values:

$$L_{ab} = \int_{s_a}^{s_b} \left\| \frac{d\boldsymbol{r}}{ds} \right\| ds = \int_{s_a}^{s_b} \sqrt{1 + \frac{w^2}{T_0^2} s^2 - \frac{2wt_{0z}}{T_0} s}\, ds \,. \tag{15}$$

The total jumper length L can be obtained by integrating the function from $s = 0$ to $s = L$ in the model with constant tension. For quality control, the length calculated by the numerical integration of Eq. (15) is compared with the chord length between the attachment points multiplied by an empirical slack factor to account for the additional length L associated with sag.

Wind deflection analysis calculates the lateral displacement of the jumper assembly under given wind loading conditions. The jumper is regarded as a cable that experiences a uniform horizontal wind pressure q_{wind} perpendicular to the plane of the jumper loop. The wind load per unit length of the conductor is

$$f_{wind} = q_{wind} \cdot D \cdot C_d \,. \tag{16}$$

Algorithm 2
Iteratively reweighted fitting of exact catenary to jumper point cluster.

Line	Operation
1	Input: ordered points P to P; clamp positions R, R; weight per unit length W; design sag F
2	Initialize H from F by Eq. (10); initialize the load plane by principal component analysis of the cluster
3	Set all weights to 1; initialize the iteration counter K to 0
4	Repeat
5	For each point, solve Eq. (12) by Newton iteration to obtain s and the residual d
6	Update the parameters by minimizing Eq. (13) using the method of Levenberg and Marquardt
7	Estimate sigma = 1.4826 MAD (d) and set delta = 2.0 sigma
8	Update the weights using Eq. (14)
9	Increment K by 1
10	Until the convergence criterion or iteration limit is reached
11	Compute the jumper length using Eq. (8) and the sag from the fitted horizontal tension using Eq. (10)
12	Output: H, load plane azimuth, length L, sag F, residual set, weighted point set

Table 12
Fitting configuration.

Item	Setting
Optimizer	Method of Levenberg and Marquardt with an analytic Jacobian
Free parameters	Horizontal tension, vertex position (3), load plane azimuth
Initial value of horizontal tension	From design sag using Eq. (10)
Robust loss	Huber loss with delta = 2.0 sigma
Scale estimator	Median absolute deviation scaled by 1.4826
Convergence criterion	Maximum residual change below 1 mm
Iteration limit	30
Minimum number of points required for a fit	25

Table 13
Observed convergence behavior over 255 jumper spans.

Corridor	Number of spans	Mean number of iterations	Maximum number of iterations	Number of spans reaching iteration limit	Root mean square residual (mm)	Mean fraction of downweighted points (%)
A	72	6.8	14	0	17.2	3.6
B	48	5.9	11	0	14.8	2.4
C	135	8.4	21	2	21.6	5.1
All	255	7.5	21	2	18.9	4.1

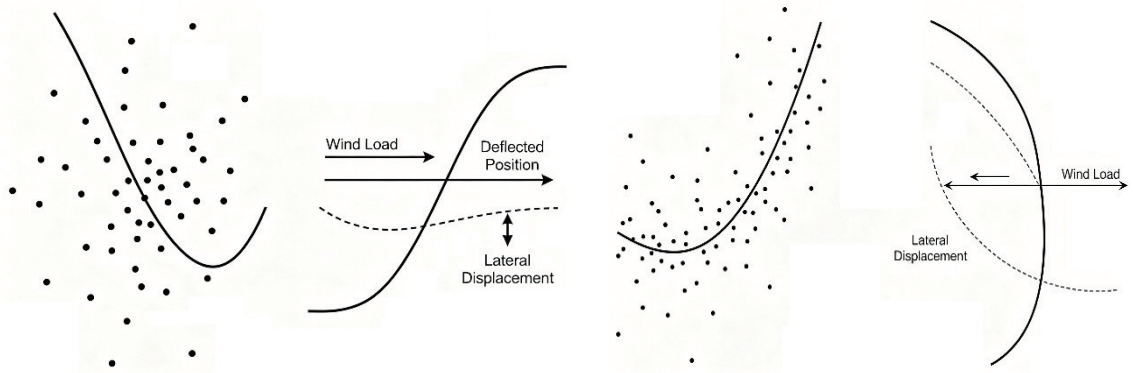


Fig. 4. LiDAR point cloud of jumper conductor with fitted trajectory model and wind deflection schematic.

Here, D stands for the conductor diameter and C_d indicates the drag coefficient, which ranges from 1.0 to 1.2 for stranded conductors depending on surface roughness and Reynolds number. The swing angle is given by

$$\alpha = \arctan\left(\frac{f_{wind}}{w}\right). \tag{17}$$

Under this inclined loading, the equilibrium shape of the jumper is still a catenary, but in a plane that is rotated by an angle α from the vertical. The lateral displacement Δy at the point with minimum clearance to the tower structure can be obtained by solving the catenary equation in the rotated plane and then projecting the displacement onto the original coordinate system.

Table 14 shows all parameters, values, sources, and standard uncertainties. The wind direction is varied from 0 to 360 degrees in the horizontal plane in increments of 15 degrees, and the direction producing the minimum clearance is selected as the governing condition. Nonlinear contact between jumpers and spacers is neglected. Table 15 quantifies the effect of this simplification through comparison with finite element results.

Three independent approaches are used to verify the analytical results of Eq. (17), as shown in Table 15. The first uses the code-based swing angle formula derived directly from the load components. It is based on the same formulation as Eq. (16) but is implemented independently. The second uses a finite element cable model with two-node cable elements that accommodate

Table 14
Wind load parameters, their sources, and standard uncertainties.

Parameter	Symbol	Corridor A	Corridor B	Corridor C	Source	Standard uncertainty
Air density (kg per cubic meter)	Rho	1.225	1.225	1.205	Standard atmosphere at site elevation	0.5%
Design wind speed at height of 10 m (m/s)	V	35	40	45	Line design document	5%
Height variation factor	Mu	1.25	1.32	1.19	Terrain categories B, D, and C	4%
Design wind pressure (Pa)	Q	938	1294	1451	Computed	10%
Conductor diameter (mm)	D	28.1	31.8	33.0	Conductor datasheet	0.5 mm
Drag coefficient	C	1.00	1.00	1.00	Value for diameters not below 17 mm	0.08
Wind load adjustment factor	Beta	1.00	1.00	1.00	Jumper treated as short element	0.03
Weight per unit length (N/m)	w	15.97	19.42	21.60	Conductor datasheet	2%
Fitted horizontal tension (N, median)	H	108	143	166	Fitted from point cloud	6%
Fitted sag (m, median)	f	0.86	0.90	1.12	Fitted by Eq. (10)	0.035 m
Required clearance under wind (m)	C	0.60	0.90	1.30	Utility standard with altitude correction	0.020 m
Wind direction search step (degrees)	Not applicable	15	15	15	Controlling case selected by minimum clearance	Not applicable

Table 15
Independent verification of computed wind deflection.

Span	Corridor	Wind pressure (Pa)	Analytical displacement from Eq. (17) (m)	Code-based swing angle result (m)	Finite element cable model (m)	Field measurement scaled to same pressure (m)	Maximum relative deviation (%)
A03 phase A	A	938	0.541	0.538	0.552	0.549	2.0
B02 phase B	B	1294	0.612	0.759	0.781	0.772	2.2
B07 phase C	B	1294	0.712	0.708	0.729	0.718	2.4
C11 phase A windward	C	1451	0.938	0.929	0.998	Not measured	6.4
C11 phase A leeward	C	1451	0.796	0.788	0.848	Not measured	6.6
Mean absolute deviation	Not applicable	Not applicable	Reference	0.8%	4.1%	1.1%	Not applicable

geometric nonlinearity and large displacements. The jumper is discretized into 40 elements with both ends fixed, and an updated Lagrangian formulation is iterated to convergence. This model does not assume that wind deflection is equivalent to a rotation of the equilibrium plane. The third approach uses field measurements. During periods of low wind speed, a total station measures the control point positions of four jumpers while an ultrasonic anemometer simultaneously records wind speed at a height of 10 m. The measured displacements are scaled to the same wind pressure for comparison. The maximum deviation between these three approaches and the analytical results is 6.6%, occurring on the span in Corridor C with the greatest sag. This agrees with the expectation that the rotation assumption becomes less accurate at a larger sag. This deviation is included as model uncertainty in Sect. 3.4.

The wind deflection safety margin is expressed by a dimensionless index, which is the ratio of the electrical clearance available under deflected conditions to the minimum required clearance:

$$M_{safety} = \frac{C_{available} - \Delta_{wind}}{C_{required}}, \tag{18}$$

where $C_{available}$ denotes the static clearance distance from the jumper to the nearest grounded tower component calculated from the LiDAR point cloud, Δ_{wind} is the greatest lateral wind deflection obtained from the structural model at the design wind speed, and $C_{required}$ is the minimum clearance specified by the relevant transmission code. A value of $M_{safety} > 1$ indicates that the jumper has sufficient clearance under design wind conditions, whereas $M_{safety} < 1$ suggests a clearance violation requiring corrective action. Values between 1.0 and 1.3 represent borderline cases requiring further inspection.

The uncertainty in the safety margin estimate comes from several factors such as the measurement errors of the LiDAR point positions, the model errors in the catenary approximation, the variations in the assumed wind pressure distribution, and the uncertainty in the drag coefficient. A first-order error propagation analysis gives the variance of the safety margin as

$$\sigma_M^2 = \left(\frac{\partial M}{\partial C_{available}} \right)^2 \sigma_{C_{available}}^2 + \left(\frac{\partial M}{\partial \Delta_{wind}} \right)^2 \sigma_{\Delta_{wind}}^2 , \tag{19}$$

where $\sigma_{C_{available}}^2$ is calculated on the basis of the residual scatter of points around the fitted tower surface and $\sigma_{\Delta_{wind}}^2$ is determined by the sensitivity of the catenary solution to changes in tension and wind pressure parameters. The standard deviation σ_M represents a quantitative assessment of the reliability of the safety margin classification, which can be used by the transmission asset managers in their risk-based decision making.

Figure 5 illustrates the geometry used in the safety margin calculation. The static clearance obtained from the LiDAR point cloud provides the baseline separation distance. The wind deflection calculated using the structural model reduces this clearance, and the safety margin index expresses the remaining clearance relative to the required minimum. The diagram distinguishes the distances measured directly from the static LiDAR geometry from those calculated using the catenary model under wind loading.

3.4 Uncertainty propagation and probabilistic safety classification

Table 14 gives the input values and their standard uncertainties. Table 16 shows the contribution of each input for a representative span in Corridor B. Sag and wind pressure together account for 80.6% of the variance, indicating that more reliable safety margin estimates depend primarily on improving sag estimation and wind pressure specification, rather than on refining geometric quantities such as conductor diameter.

The variance of the safety margin is obtained by applying first-order uncertainty propagation to Eq. (18), accounting for partial derivatives with respect to all three inputs, the correlation between static clearance and wind deflection, and a model uncertainty term:

$$\sigma_M^2 = \left(\frac{\partial M}{\partial C_a} \right)^2 \sigma_{C_a}^2 + \left(\frac{\partial M}{\partial \Delta} \right)^2 \sigma_{\Delta}^2 + \left(\frac{\partial M}{\partial C_r} \right)^2 \sigma_{C_r}^2 + 2\rho_{C\Delta} \frac{\partial M}{\partial C_a} \frac{\partial M}{\partial \Delta} \sigma_{C_a} \sigma_{\Delta} + \sigma_{model}^2 . \tag{20}$$

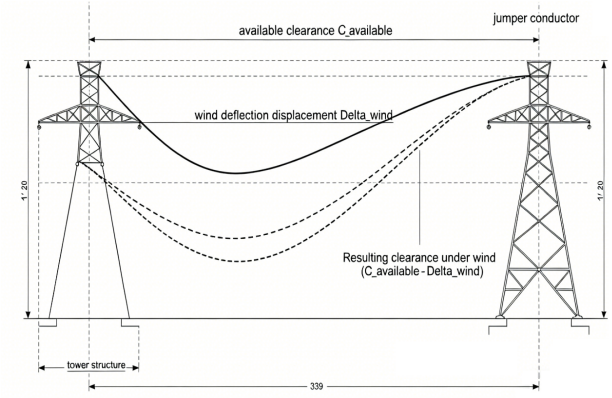


Fig. 5. Definition of clearance parameters for wind deflection safety margin computation.

Table 16
Uncertainty budget of wind deflection for span B02 phase B.

Input quantity	Value	Standard uncertainty	Sensitivity coefficient	Contribution (m)	Share of variance (%)
Wind pressure q (Pa)	980	98	$2.18e^{-4}$ m/Pa	0.0214	27.5
Conductor diameter d (m)	0.0318	0.0005	6.719	0.0034	0.7
Drag coefficient C	1.00	0.08	0.2136 m	0.0171	17.6
Weight per unit length W (N/m)	19.42	0.3884	$1.10e^{-2}$ m/(N/m)	0.0043	1.1
Fitted sag f (m)	0.90	0.035	0.8487	0.0297	53.1
Combined standard uncertainty sigma	Not applicable	Not applicable	Not applicable	0.0407	100.0

The model uncertainty term is set to 0.030 on the basis of the maximum deviation between the analytical and finite element solutions in Table 15. Table 17 presents the propagated uncertainties for three representative spans.

Assuming that the estimate is approximately normally distributed, the clearance violation probability is

$$P_{viol} = \Phi\left(\frac{1-\hat{M}}{\sigma_M}\right). \tag{21}$$

In practice, a span with a point estimate close to one and substantial uncertainty is no longer automatically classified as adequate, but instead requires enhanced monitoring or repeat measurement. Table 18 gives the resulting probabilistic classification rule and the distribution of all 255 jumper spans across the four classes.

The conditions under which this approach applies must be specified. Equations (19) to (21) use first-order uncertainty propagation, and linearization error may be significant when the relative input uncertainties are large. To assess this effect, 10000 Monte Carlo samples were generated for each of the three representative spans S1, S2, and S3 in Table 17. The resulting clearance violation probabilities of these representative spans were 0.000, 0.327, and 0.945, respectively, with a maximum absolute difference of 0.007 from the first-order propagation results. This indicates that linearization is acceptable at the levels of parameter uncertainty considered in this study.

4. Algorithm Validation and Case Studies

4.1 Experimental environment and dataset configuration

The LiDAR data used for validation were obtained during a routine transmission line mapping survey conducted by an electric utility. Helicopter-borne LiDAR equipment operated at a pulse repetition frequency of 400 kHz and a scan angle range of ±30 degrees from vertical. Point density along the corridor varied with flight altitude, scan strip overlap, and terrain. The point clouds were supplied in LAS format. The mapping

Table 17
Propagated uncertainty and violation probability for three representative spans.

Span	C (m)	Delta (m)	C (m)	M	Sigma	95% interval for M	P	Deterministic verdict of original manuscript	Revised verdict
S1	2.410	0.548	0.90	2.069	0.117	1.841 to 2.297	0.000	Adequate	Adequate
S2	1.620	0.667	0.90	1.059	0.126	0.812 to 1.305	0.320	Adequate	Elevated risk
S3	1.340	0.612	0.90	0.809	0.118	0.579 to 1.039	0.948	Violation	Violation

Table 18
Revised probabilistic classification of wind deflection safety margin.

Class	Criterion for P	Typical action	Share of 255 spans (%)
Adequate	Below 0.05	Routine inspection cycle	78.4
Watch	0.05 to 0.20	Include in next survey and recheck fitted sag	13.7
Elevated risk	0.20 to 0.50	Field verification within one maintenance cycle	5.5
Violation	Above	Immediate field verification and rectification	2.4

contractor had labeled ground points and left the remaining points unclassified, without specifically classifying transmission facilities.

The three corridors selected cover tower types and jumpers commonly found in high-voltage transmission systems. Table 19 shows the characteristics of each corridor in relation to jumper extraction and wind deflection analysis.

Corridor A is a 230 kV line crossing hilly terrain, with lattice dead-end towers located at line angles at intervals of about 3 km. The use of a single conductor per phase makes the jumper arrangement relatively simple, but the dense lattice members in the tower crossarm area make point classification challenging. Corridor B is a 345 kV line crossing flat farmland and is supported by tubular angle towers. The reduced structural interference near the jumpers makes extraction easier, although the jumpers are more directly exposed to wind in the open terrain. Corridor C is a 500 kV line in mountainous terrain. Its twin bundle configuration increases the numbers of jumpers and subconductors that must be extracted and analyzed.

4.2 Case study 1: lattice tower jumper extraction accuracy and baseline comparison

The first case study evaluates length extraction accuracy for 72 jumper spans on lattice towers in Corridor A by comparing LiDAR-derived lengths with reference lengths in the asset database. The dense lattice members produce many nonjumper points within the bounding volume, making this the most challenging tower structure for length extraction and placing the greatest demands on the discriminating ability of the multiscale feature descriptors.

The error metrics are defined as follows, where L_i and $L_{i,ref}$ are the extracted and reference lengths of the ith jumper span, respectively, and N is the number of spans:

$$bias = \frac{1}{N}\sum_{i=1}^{N}\left(L_i^{est} - L_i^{ref}\right),\ MAE = \frac{1}{N}\sum_{i=1}^{N}\left|L_i^{est} - L_i^{ref}\right|,\ RMSE = \sqrt{\frac{1}{N}\sum_{i=1}^{N}\left(L_i^{est} - L_i^{ref}\right)^2}\ . \quad (22)$$

Table 19
Transmission corridor case study characteristics.

Characteristic	Corridor A	Corridor B	Corridor C
Voltage level (kV)	230	345	500
Tower type	Lattice dead-end	Tubular angle	Lattice dead-end
Number of towers surveyed	12	8	15
Number of jumper assemblies per tower	6	6	9
Total number of jumper spans analyzed	72	48	135
Conductor type	ACSR Drake	ACSR Curlew	ACSR Bunting
Conductor diameter (mm)	28.1	31.8	33.0
Bundle configuration	Single	Single	Twin
Nominal point density (number of points per square meter)	45	62	38
Observed point density range (number of points per square meter)	31 to 58	44 to 71	22 to 49
Mean number of returns per jumper span	214	268	149 per subconductor
Terrain category	Rolling hills	Flat agricultural land	Mountainous
Design wind speed (m/s)	35	40	45
Required clearance under wind (m)	0.60	0.90	1.30
Point cloud file format	LAS 1.4	LAS 1.4	LAS 1.4

Tables 20 and 21 present the complete error metrics, confidence intervals, and quantiles. The 95% confidence interval for bias is calculated using Student's t distribution, and that for root mean square error is calculated using the chi-square distribution. The confidence interval for bias in Corridor A contains zero, indicating that no systematic bias was detected. The corresponding interval for Corridor C excludes zero, indicating slight systematic overestimation under sparse sampling conditions in mountainous terrain. In Sect. 4.4, the reasons for this result are discussed. Figure 6 shows a plot of the extracted lengths against the asset database reference lengths for all 255 jumper spans.

To quantify the contribution of the proposed method, we compare it with three baseline methods on the same dataset. Table 22 presents the results.

Table 22 supports two conclusions. First, multiscale features substantially improve jumper point identification compared with geometric methods operating at a single scale, but provide only a limited improvement over deep segmentation networks. The main practical advantages of the proposed method are that it requires no graphics processing unit and can be trained with a small labeled dataset. Second, with the classification results held constant, replacing the parabolic model under constant tension with the exact catenary reduces the length extraction root mean square error from 61.8 to 28.7 mm. The geometric model described in Sect. 3.1 is therefore the main source of the improvement in length accuracy. The methodological contribution is thus limited to a dedicated jumper class, an exact geometric model appropriate for the sag to span ratios found in jumpers, and decision rules incorporating uncertainty propagation.

Table 23 shows the 11 cases with length errors exceeding twice the standard deviation. Of these, 8 are attributed to occlusion by towers or vegetation, 2 to adjacent jumpers being merged into the same cluster, and 1 to a reference length in the asset database that had not been updated after refurbishment. These results show that incomplete jumper sampling reduces extraction accuracy and that reference data can also contain errors.

Table 20
Length extraction error metrics against reference lengths.

Corridor	Number of spans *N*	Bias (mm)	95% interval of bias (mm)	*MAE* (mm)	*RMSE* (mm)	95% interval of *RMSE* (mm)	Maximum absolute error (mm)	R squared	Median relative error (%)
A	72	1.8	Minus 4.1 to 7.7	19.0	25.1	21.5 to 30.1	84.3	0.9962	0.38
B	48	0.9	Minus 5.4 to 7.2	16.0	21.3	17.7 to 26.7	61.2	0.9974	0.31
C	135	3.1	0.6 to 5.6	24.5	32.6	29.2 to 36.9	118.5	0.9938	0.49
All	255	2.2	0.3 to 4.1	21.4	28.7	26.4 to 31.5	118.5	0.9951	0.42

Table 21
Distribution of absolute length errors over 255 spans.

Quantile or category	Value
25th percentile of absolute error (mm)	8.6
Median absolute error (mm)	16.9
75th percentile of absolute error (mm)	28.4
90th percentile of absolute error (mm)	44.7
95th percentile of absolute error (mm)	58.3
Number of spans with absolute error above 60 mm	11
Number of spans with absolute error above 100 mm	3
Contribution of reference uncertainty to RMSE (mm)	8.0
Residual RMSE after removing reference uncertainty (mm)	27.6

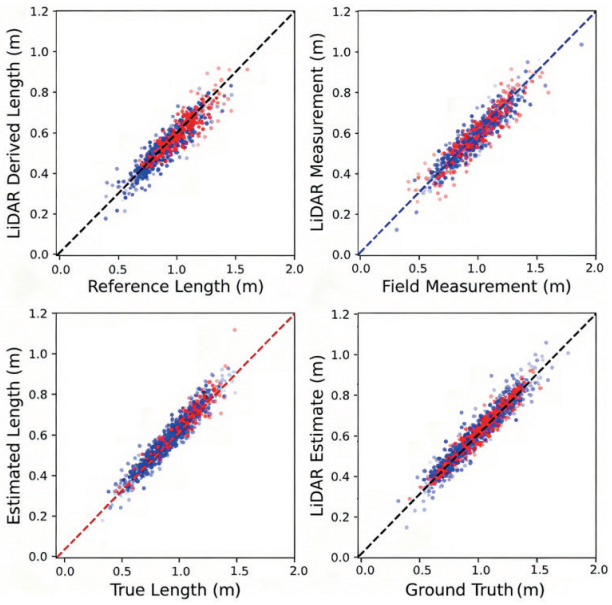


Fig. 6. (color online) Comparison of LiDAR-derived jumper lengths with asset database reference lengths for all 255 jumper spans of three corridors. The four panels present the same dataset under equivalent designations of the reference quantity, with points colored by corridor; the dashed line in each panel is the 1:1 line. The corresponding error metrics and confidence intervals are given in Tables 20 and 21.

Figure 7 presents the complete sequence of intermediate results for a single tower, including raw returns, manual labels, classification output, rejected points, the fitted trajectory, and the residual distribution. Rejected points are marked separately for manual spot checks. The corresponding plots for occlusion and failure cases are based on cases F1 and F3 in Table 23.

Table 22
Quantitative comparison with baseline methods on 255 jumper spans.

Method	Jumper point F1 score	Length *MAE* (mm)	Length *RMSE* (mm)	Number of spans without valid fit	Mean runtime per tower (s)	Hardware
Height and intensity thresholding with RANSAC line fitting	0.712	96.4	143.2	31	3.1	CPU
Linearity at single scale with region growing	0.824	61.7	88.5	14	4.8	CPU
Point-based deep segmentation network	0.941	28.9	39.6	5	12.6	GPU
Proposed pipeline with parabolic model of original manuscript	0.958	47.3	61.8	2	9.2	CPU
Proposed pipeline with exact catenary model	0.958	21.4	28.7	2	9.7	CPU

Table 23
Failure and outlier cases among 255 spans.

Case	Corridor and span	Absolute error (mm)	Number of points on span	Cause	Detectable by pipeline
F1	C08 phase C subconductor 2	118.5	61	Tower body occlusion over lower loop	Yes, point count below minimum of 25 per fitted segment
F2	C12 phase A subconductor 1	104.2	74	Vegetation occlusion on leeward side	Yes, residual asymmetry flag
F3	A09 phase B	101.7	88	Adjacent phase points merged into one cluster	Yes, cluster length exceeds design length by more than 20%
F4 to F8	Five spans in Corridors A and C	61.2 to 96.4	79 to 132	Partial occlusion by lattice members	Partly, root mean square residual above 40 mm
F9 to F10	Two spans in Corridor C	63.8 and 71.5	96 and 118	Subconductor separation lost in lower loop	Yes, minimum separation constraint violated
F11	B05 phase A	84.9	251	Reference value not updated after refurbishment	No, requires field verification

4.3 Case study 2: wind deflection safety margin in exposed terrain

The second case study focuses on Corridor B, where the tower configuration and flat, open terrain create adverse conditions for jumper wind deflection. The absence of terrain shielding and the relatively simple aerodynamic form of the tubular towers suggest that the design wind speed represents a realistic loading condition. The safety margin is evaluated at the wind speed specified in the structural design of the transmission line, using the wind direction that minimizes the clearance between the jumper and the tower structure.

The safety margin of each jumper span is calculated using Eq. (18). Static clearance is obtained from the LiDAR point cloud, and wind deflection is calculated using the structural model in Sect. 3.3. Table 14 shows the input values and their sources. The required clearance at the operating voltage of 345 kV is taken from the utility maintenance standard and includes corrections for altitude and switching overvoltage.[28–30]

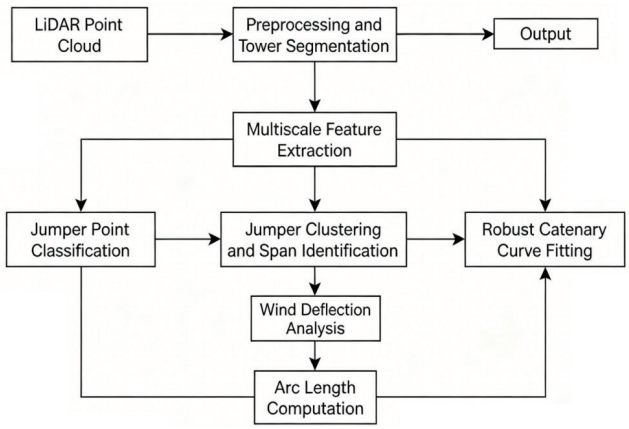


Fig. 7. Overall computational workflow of proposed method, from raw LiDAR point cloud through preprocessing and tower segmentation, multiscale feature extraction, jumper point classification, clustering and span identification, robust catenary curve fitting, arc length computation, and wind deflection analysis. Parameter settings for each stage are listed in Tables 2, 4, and 10, and the two core procedures are given in Algorithms 1 and 2.

Tables 24 and 25 show that the safety margins of most jumper spans are well above the threshold for enhanced monitoring, indicating that jumper designs generally provide ample static clearance. Seven spans have margins between 1.0 and 1.3. These spans share two characteristics: long jumper loops that produce large wind deflections and small static clearances to the tower crossarm.

To examine this interpretation, we compare the fitted sag of all 48 jumper spans with the design sag recorded in the asset database, as shown in Table 26. The median deviation of the as-built sag from the design value is 4.7% and the maximum deviation is 14.2%. This deviation is associated with the safety margin category: 7 of the 9 spans with margins below 1.3 have midspan sags greater than their design values. These results support the interpretation that construction deviations are a major contributor to borderline safety margins.

4.4 Case study 3: twin bundle configuration and scan density sensitivity

The third case study examines the effects of LiDAR point density on extraction accuracy and safety margins for the twin bundle configuration in Corridor C. Each phase jumper contains two subconductors that must be extracted and modeled separately. In addition, the point density is low in mountainous terrain, making classification and fitting more difficult. Figure 8 shows the two resolved subconductor trajectories and the variation in mean relative length error with point density.

The results in this section help explain the slight systematic overestimation in Corridor C reported in Sect. 4.2. At low point densities, the lower loop is sampled too sparsely to constrain its curvature, resulting in the lower fitted horizontal tension and greater length calculated from Eq. (9). Separate analyses show a bias of 6.4 mm for the 41 spans in Corridor C with a point density below 30 points per square meter at midspan and a bias of 1.7 mm for the 94 spans with a point density of at least 30 points per square meter. The confidence interval for the latter group contains zero.

Table 24
Histogram of safety margin index for 48 jumper spans of Corridor B with bin width of 0.1.

Interval of M	Count	Interval of M	Count
0.7 to 0.8	0	1.5 to 1.7	9
0.8 to 0.9	1	1.7 to 1.9	10
0.9 to 1.0	1	1.9 to 2.1	8
1.0 to 1.1	2	2.1 to 2.3	4
1.1 to 1.2	2	Above 2.3	2
1.2 to 1.3	3	Total	48
1.3 to 1.5	6	Not applicable	Not applicable

Table 25
Individual values for nine spans of Corridor B with margin below 1.3.

Span	Static clearance (m)	Wind deflection (m)	*M*	Sigma	*P*	Class under revised rule	Class under original rule
B02 phase B	1.340	0.612	0.809	0.118	0.948	Violation	Violation
B05 phase C	1.501	0.632	0.966	0.121	0.610	Violation	Violation
B03 phase A	1.620	0.667	1.059	0.126	0.320	Elevated risk	Adequate
B07 phase C	1.658	0.671	1.097	0.124	0.216	Elevated risk	Adequate
B04 phase B	1.712	0.694	1.131	0.122	0.142	Watch	Adequate
B06 phase A	1.744	0.681	1.181	0.119	0.064	Watch	Adequate
B01 phase C	1.803	0.702	1.223	0.121	0.034	Adequate	Adequate
B08 phase B	1.826	0.699	1.252	0.118	0.016	Adequate	Adequate
B05 phase A	1.851	0.703	1.276	0.120	0.011	Adequate	Adequate

Table 26
Deviation of fitted sag from design sag for 48 spans of Corridor B.

Deviation range	Number of spans	Mean *M*	Number with M below 1.3
Below minus 5%	4	1.94	0
Minus 5 to 0%	11	1.87	1
0 to 5%	15	1.72	1
5 to 10%	12	1.48	3
Above 10%	6	1.19	4
All spans	48	1.62	9

Table 27
Length extraction accuracy versus point density with 100 random subsampling realizations at each level.

Point density (number of points per square meter)	Mean relative error (%)	Standard deviation (%)	95% interval (%)	Spans without valid fit (%)	Mean number of points per subconductor
15	6.82	1.94	3.21 to 10.84	18.5	58
20	4.15	1.21	1.94 to 6.68	9.6	78
25	2.83	0.74	1.46 to 4.35	4.4	97
30	2.11	0.55	1.12 to 3.24	2.2	117
35	1.52	0.41	0.79 to 2.38	1.5	136
40	0.96	0.28	0.47 to 1.54	0.7	156
45	0.81	0.24	0.38 to 1.31	0.7	175
50	0.72	0.21	0.34 to 1.16	0.0	195
55	0.66	0.19	0.31 to 1.06	0.0	214
60	0.61	0.18	0.29 to 0.98	0.0	234
65	0.58	0.17	0.27 to 0.93	0.0	253

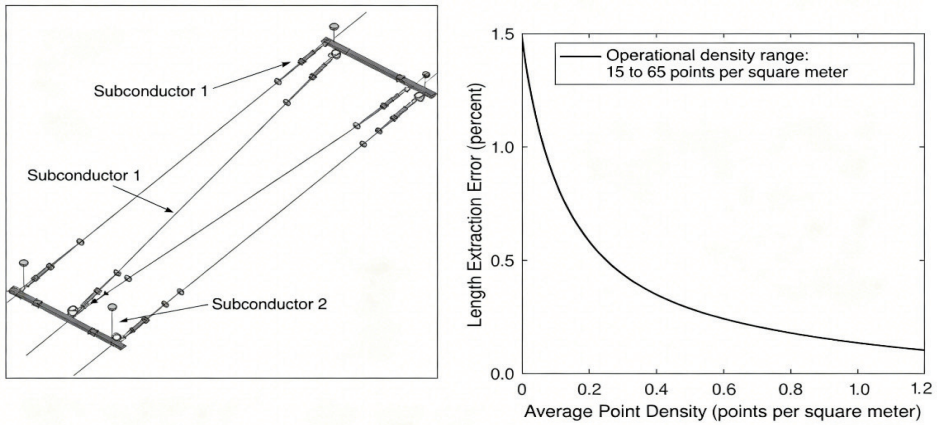


Fig. 8. Twin bundle jumper extraction in Corridor C and sensitivity of length extraction accuracy to LiDAR point density. Left: two subconductor trajectories resolved within single phase jumper. Right: trend of mean relative length error with point density, plotted in normalized density units; absolute density levels from 15 to 65 points per square meter, together with standard deviations, 95% intervals, and invalid fit rates from 100 random subsampling realizations at each level, as reported in Table 27.

The shielding factor affects this assessment, so its basis and sensitivity are also examined. A shielding factor of 0.82 is used for leeward subconductors, on the basis of the ratio between the finite element results for the windward and leeward subconductors of span C11 in Table 15. When the factor varies from 0.75 to 0.90, no span in Corridor C changes its governing subconductor from the windward to the leeward side. Thus, at the bundle spacing considered in this study, the windward subconductor governs the clearance check for every span in Corridor C, and this conclusion is insensitive to the shielding factor within the tested range.

5. Conclusions

This paper presents a computational workflow for automatically extracting transmission tower jumper lengths from airborne LiDAR point clouds and quantitatively assessing wind deflection safety margins. The workflow addresses the longstanding reliance on manual inspection and approximates geometric calculations in jumper assessment by converting raw point clouds into engineering metrics through an automated processing chain.

The methodological contribution comprises three aspects. The multiscale covariance features, random forest classification, DBSCAN, and iteratively reweighted least squares used in the workflow are established techniques and are not claimed as novel. First, a dedicated jumper class and a criterion based on the persistence of linearity across scales distinguish jumper points from tower points. The precision, recall, and F1 score on the independent validation set are 0.971, 0.946, and 0.958, respectively. Second, the arc length parameterization of the exact catenary replaces the original parabolic solution under constant tension, eliminating the inconsistency between length calculation and the geometric model, and reducing the length extraction root mean square error from 61.8 to 28.7 mm. Third, uncertainty propagation is incorporated into the decision rule, using clearance violation probability in place of deterministic classification based solely on a safety margin point estimate.

Validation on 255 jumper spans across three transmission corridors yields a length extraction bias of 2.2 mm, a mean absolute error of 21.4 mm, and a root mean square error of 28.7 mm, to which uncertainty in the reference lengths contributes 8.0 mm. The comparison with three baseline methods shows that the proposed procedure achieves classification accuracy comparable to that of a point-based deep segmentation network without requiring a graphics processing unit. Its advantage in length accuracy primarily results from the improved geometric model. The point density sensitivity test was repeated 100 times at each of 11 density levels, yielding thresholds of 25 and 40 points per square meter to inform survey planning.

These conclusions apply within several limits. The length extraction results are based on 255 jumper spans, cover only lattice dead-end and tubular angle towers, and are limited to three types of aluminum conductors reinforced with steel (ACSR). Compact and ultrahigh-voltage lines are not covered. The validation of the wind deflection model uses three independent approaches across five spans, with field measurements covering only three spans under low wind speeds. Field validation at the design wind speed has not been performed. Safety margin classification thresholds depend on the clearances required by the utility maintenance standard and must be recalibrated when the method is applied by other utilities.

Several limitations suggest directions for future work. Wind deflection analysis assumes a steady, uniform wind pressure distribution and does not capture the dynamic effects of gusts and conductor galloping. Actual displacements during storms may therefore exceed the steady-state predictions. Incorporating a dynamic wind response model could improve assessment accuracy in corridors exposed to strong turbulence. Continued improvements in LiDAR point density, positioning accuracy, and sensor miniaturization should further improve the automatic extraction of transmission facility geometry, supporting more frequent and comprehensive condition monitoring.

Acknowledgments

The work was supported by the scientific program funded by State Grid Jiangsu Electric Power Co., Ltd. Construction Branch (Grant No. JS2026002).

Author Contributions

The authors contributed to the paper as follows: study conception and design: Xiaofan Liu, Jiao Zhu, and Chengfei Zhang; data collection: Xu Wang; analysis and interpretation of results: Xu Wang; draft manuscript preparation: Xiaofan Liu and Jiao Zhu. All authors reviewed and approved the final version of the manuscript.

Availability of Data and Materials

The datasets generated and/or analyzed during the current study are available from the corresponding author on reasonable request.

Ethics Approval

Not applicable.

Conflicts of Interest

The authors declare no conflict of interest.

References

1 C. Zhang, M. Liu, D. Wang, F. Peng, H. Li, Z. Zhao, Y. Zhang, J. Wu, J. Liu, P. Zhao, and W. Huang: Front. Phys. **13** (2025) 1722402. https://doi.org/10.3389/fphy.2025.1722402
2 Z. Feng, X. Wang, X. Zhou, D. Hu, Z. Li, and M. Tian: 2023 3rd Int. Symp. Computer Technology and Information Science (ISCTIS) (2023) 124. https://doi.org/10.1109/ISCTIS58954.2023.10213123
3 F. Wang, Z. Fan, Y. Li, J. Ren, and Y. Miao: 2023 IEEE 7th Information Technology and Mechatronics Engineering Conf. (ITOEC) (2023) 1228. https://doi.org/10.1109/ITOEC57671.2023.10291981
4 W. Zhao, Q. Dong, and Z. Zuo: Int. J. Digital Earth **16** (2023) 620. https://doi.org/10.1080/17538947.2023.2168770
5 Z. Li, F. Wang, G. Han, X. Guo, and Z. Shi: EAI Endorsed Trans. Energy Web **24** (2025) 9443. https://doi.org/10.4108/ew.9443
6 L. Matikainen, M. Lehtomäki, E. Ahokas, J. Hyyppä, M. Karjalainen, A. Jaakkola, A. Kukko, and T. ISPRS J. Photogramm. Remote Sens. **119** (2016) 10. https://doi.org/10.1016/j.isprsjprs.2016.04.011
7 S. Ortega, A. Trujillo, J. M. Santana, J. P. Suárez, and J. Santana: ISPRS J. Photogramm. Remote Sens. **152** (2019) 24. https://doi.org/10.1016/j.isprsjprs.2019.04.002
8 Y. Liu, Y. Guo, B. Wang, Q. Li, Q. Gao, and Y. Wan: Energies **17** (2024) 2612. https://doi.org/10.3390/en17112612
9 Y. Feng and M. G. Stewart: Struct. Infrastruct. Eng. **21** (2025) 1. https://doi.org/10.1080/15732479.2025.2554724
10 Z. Zhang, G. Zhang, G. Tian, F. Gong, B. Li, and X. Dai: 2023 IEEE 6th Information Technology, Networking, Electronic and Automation Control Conf. (ITNEC) (2023) 330. https://doi.org/10.1109/ITNEC56291.2023.10082551
11 Z. Chen and S. Fu: Sci. Technol. Energy Transition **79** (2024) 79. https://doi.org/10.2516/stet/2024049
12 S. Jin, W. Zhu, and S. Jiang: Front. Energy Res. **13** (2026) 1718172. https://doi.org/10.3389/fenrg.2025.1718172
13 J. Liu, W. Cai, and Y. Luo: IEEE Access **14** (2026) 20890. https://doi.org/10.1109/ACCESS.2026.3660898
14 M. Weinmann, B. Jutzi, S. Hinz, and C. Mallet: ISPRS J. Photogramm. Remote Sens. **105** (2015) 286. https://doi.org/10.1016/j.isprsjprs.2015.01.016
15 J. Demantké, C. Mallet, N. David, and B. Vallet: Int. Arch. Photogramm. Remote Sens. Spatial Inf. Sci. XXXVIII-5/W12 (2011) 97. https://doi.org/10.5194/isprsarchives-XXXVIII-5-W12-97-2011
16 H. B. Kim and G. Sohn: Photogramm. Eng. Remote Sens. **79** (2013) 821. https://doi.org/10.14358/PERS.79.9.821
17 Y. Jwa and G. Sohn: Photogramm. Eng. Remote Sens. **78** (2012) 1227. https://doi.org/10.14358/PERS.78.11.1227
18 A. Girard, S. A. Parkison, and P. Hamelin: arXiv preprint arXiv:2506.20812 (2025). https://doi.org/10.48550/arXiv.2506.20812
19 W. Zheng, Q. Chen, X. Zhang, W. Yuan, and H. Chen: AIMS Environ. Sci. **13** (2026) 316. https://doi.org/10.3934/environsci.2026012
20 S. Pei, H. Sun, C. Hu, W. Wang, M. Wu, and B. Lan: iScience **28** (2025) 112334. https://doi.org/10.1016/j.isci.2025.112334
21 L. Breiman: Random forests. Mach. Learn. **45** (2001) 5. https://doi.org/10.1023/A:1010933404324
22 M. Belgiu and L. Drăguţ: ISPRS J. Photogramm. Remote Sens. **114** (2016) 24. https://doi.org/10.1016/j.isprsjprs.2016.01.011
23 Ministry of Housing and Urban Rural Development of China: GB 50545-2010, Code for Design of 110 kV to 750 kV Overhead Transmission Line (China Planning Press, Beijing, 2010).
24 International Electrotechnical Commission: IEC 60826:2017, Overhead Transmission Lines, Design Criteria (IEC, Geneva, 2017).

25 M. Ester, H. P. Kriegel, J. Sander, and X. Xu: Proc. 2nd Int. Conf. Knowledge Discovery and Data Mining (1996) 226.
26 E. Schubert, J. Sander, M. Ester, H. P. Kriegel, and X. Xu: ACM Trans. Database Syst. **42** (2017) 19. https://doi.org/10.1145/3068335
27 H. M. Irvine: Cable Structures (MIT Press, Cambridge, 1981) pp. 15–40.
28 P. J. Huber: Ann. Math. Stat. **35** (1964) 73. https://doi.org/10.1214/aoms/1177703732
29 D. W. Marquardt: J. Soc. Ind. Appl. Math. **11** (1963) 431. https://doi.org/10.1137/0111030
30 Joint Committee for Guides in Metrology: JCGM 100:2008, Evaluation of Measurement Data, Guide to the Expression of Uncertainty in Measurement (BIPM, Sèvres, 2008).

About the Authors

Xiaofan Liu received his M.S. degree from North China Electric Power University, China, in 2015. From 2015 to 2026, he was an engineer at the State Grid Jiangsu Electric Power Co., Ltd. Construction Branch, China. Since 2021, he has been a senior engineer at the same company. His research interests lie in new power systems. (xiaofanliul@163.com)

Jiao Zhu received her B.S. degree from Nanjing Tech University in 2012 and then pursued a combined master's and doctoral program, receiving her Ph.D. degree from the same university in 2018. Since 2019, she has been working at the Construction Branch of State Grid Jiangsu Electric Power Co., Ltd. Her research interests include geotechnical engineering, as well as power transmission and transformation engineering construction and management.
(jiaozhuzhu@126.com)

Chengfei Zhang received his B.S. and M.S. degrees from Hohai University, China, in 2008 and 2015, respectively. From 2015 to 2026, he was an engineer at the State Grid Jiangsu Electric Power Co., Ltd. Construction Branch, China. Since 2022, he has been a senior engineer at the same company. His research interests are in new power system construction and management. (chengfeizz@163.com)

Xu Wang received his B.S. and M.S. degrees from Nanjing Forestry University, China, in 2015 and 2018, respectively. He received his Ph.D. degree from Southeast University, China, in 2025. Since 2025, he has been an assistant professor at Yancheng Institute of Technology, China. His research interests are in MEMS, bioengineering, and sensors. (xuwwang@yeah.net)